

Critical magnetic fields and electron pairing in magic-angle twisted bilayer graphene

Wei Qin ^{*}, Bo Zou ^{*}, and Allan H. MacDonald[†]

Department of Physics, The University of Texas at Austin, Austin, Texas 78712, USA



(Received 28 December 2022; accepted 4 January 2023; published 26 January 2023)

The velocities of the quasiparticles that form Cooper pairs in a superconductor are revealed by the upper critical magnetic field. Here we use this property to assess superconductivity in magic-angle twisted bilayer graphene (MATBG), which has been observed over a range of moiré band-filling, twist angle, and screening environment conditions. An average Fermi velocity can be defined as $v_F^* \equiv k_B T_c \ell_c / \hbar$, where T_c and ℓ_c are the critical temperature and magnetic length, respectively. An advantage of this definition is that v_F^* can be directly extracted from the existing experimental data. Mean-field theory calculations of upper critical fields in model superconductors are consistent with the expectation that Fermi velocities defined in this way are nearly independent of the strength of pairing interaction. Moreover, for fixed strength pairing interaction, minima in v_F^* as a function of band filling are coincident with maxima in T_c , as expected from the McMillan formula. Since no association between T_c maxima and v_F^* minima is present in MATBG experimental data, we argue that the pairing interaction in MATBG is strongly filling-factor dependent. Any theory of MATBG superconductivity must explain this dependence, which is apparently primarily responsible for the observed superconducting domes.

DOI: [10.1103/PhysRevB.107.024509](https://doi.org/10.1103/PhysRevB.107.024509)

I. INTRODUCTION

The observation of superconducting domes near correlated insulating states in magic-angle twisted bilayer graphene (MATBG) [1,2] has stimulated interest in achieving a full microscopic understanding of this relatively simple electronic system [3–20]. The electronic properties of MATBG devices are extremely sensitive to multiple tuning knobs, especially electrostatic doping and twist angle [1,2,9], but also interlayer separation [3,21], vertical displacement field [3], and three-dimensional screening environment [22–24]. The tunability of MATBG makes it a particularly appealing experimental platform for the exploration of strong-correlation superconductivity.

In MATBG, as in many other superconductors, observations that clearly distinguish between purely electronic pairing mechanisms, possibly related to the correlated insulating states [25–36], and conventional phonon-mediated electron pairing [37–39] are sparse. A possible difference between purely electronic and electron-phonon mechanism of superconductivity is that in the former case the effective pairing interaction is likely to be flat-band-filling dependent [30–33]. For example, pseudospin paramagnon-mediated effective interactions tend to be enhanced close to half band fillings [40].

Since the superconducting critical temperature T_c is determined by the product of the Fermi-level density of states and the strength of pairing interaction, an accurate determination of the electronic structure is extremely helpful for identifying the microscopic pairing mechanisms. However, in contrast to

conventional metals, the electronic structure of the flat bands in MATBG is so sensitive to the details of model parameters and also to dielectric screening environment that it is difficult to draw conclusions. This is especially true when the ubiquity of Fermi-surface reconstructions related to broken flavor symmetries is acknowledged [41–43]. Therefore, detailed band structure properties are not easily predicted theoretically, and are in all likelihood device dependent.

In this work, we show that the key Fermi-level band structure properties can be determined experimentally by combining measured T_c and critical perpendicular magnetic field H_{c2} to determine the average Fermi velocity $v_F^* \equiv k_B T_c \ell_c / \hbar$ of the quasiparticles that form Cooper pairs. Here $\ell_c = \sqrt{\Phi_0 / 2\pi H_{c2}}$ with the superconducting flux quantum $\Phi_0 = 2e/hc$. Such a definition is motivated by the observation that superconductivity is suppressed at finite pairing momentum $q = 1/\ell$ because the electrons that form Cooper pairs differ in energy by $\sim (d\epsilon_k/dk)/\ell \sim \hbar v_F / \ell$, and that it is lost in mean-field theory when this difference is comparable to $k_B T_c$. Microscopically, superconductivity is lost in a magnetic field because Landau-level Cooper pair states are formed from individual electron states that differ in energy by $\sim \hbar v_F / \ell_c$ [44].

Both T_c and H_{c2} can be calculated within mean-field theory by realizing that the maximum pairing momentum $q_c = 1/\ell_c$ (see Appendix B), enabling close comparisons between experimental and theoretical results for v_F^* . For a pairing interaction that is independent of band filling, e.g., optical-phonon-mediated pairing, our calculations show that the T_c exhibits a correlation with v_F^* that is opposite to that seen in experiment. Specifically, a robust correlation between T_c maxima and v_F^* minima occurs in theory when the Fermi level is close to the van Hove singularity (VHS) of density of states.

^{*}weiqin@utexas.edu

[†]macdpc@physics.utexas.edu

TABLE I. Experimental results for the superconducting critical temperature T_c , critical perpendicular magnetic field H_{c2} , Pauli limit H_p , and the extracted average Fermi velocity v_F^* for MATBG in a variety of experiments with different twist angles θ , band fillings ν , and screening environments.

θ ($^\circ$)	ν	T_c (K)	H_{c2} (mT)	H_p (T)	v_F^* (10^4 m/s)	Ref.
1.05	-2.02	1.7		3.15		[1]
1.16	-2.15	0.5	125	0.93	0.34	
1.27	-2.33	3.1	210	5.74	1.54	[3]
1.27	-2.62	2	72	3.7	1.78	
	-2.31	3.1	180	5.74	1.67	[9]
1.1	-1	0.14	100	0.26	0.10	
	0.67	0.16	300	0.3	0.07	
	1.48	0.65	400	1.2	0.23	
1.15	-1.6	0.92	220	1.7	0.46	[22]
	1.8	0.42	26	0.78	0.56	
1.04	-2.43	1.3	>50	2.41	<1.38	[23]
1.09	-2.79	2.5	45	4.63	2.78	
1.18	-2.5	0.7	>60	1.3	<0.68	
1.12	-2.47	4	>50	7.4	<4.24	

These findings are also valid for Bistritzer-MacDonald (BM) models that account for nonlocal interlayer tunneling and Hartree-Fock self-energy corrections. In experiment, however, it appears that moving closer to van Hove singularities is actually associated with a suppression of superconducting T_c 's [20,45–47], which argues against conventional phonon-mediated pairing.

Table I summarizes experimental data and extracted v_F^* for MATBG superconductors. We note that the experimental values of v_F^* in Table I are typically 100 or more times smaller than the Dirac velocities of isolated graphene sheets, demonstrating the crucial role of the dramatically flattened moiré bands [48]. The main point we wish to make here, however, is that experimental critical temperature maxima, which always occur in a narrow range of filling factor near $\nu = -2.3$ [1,3,9,19,23], do not correlate with average Fermi velocity minima as they would in any theory in which pairing is mediated by phonons, or other bosons that are insensitive to ν .

This paper is organized as follows. In Sec. II, we introduce the band structure model, the Hartree-Fock self-energy correction, and the pairing interaction model employed in this study. In Sec. III, we briefly describe microscopic mean-field calculations of critical temperatures and critical magnetic fields. In Sec. IV, we present the main results of this work, contrasting the experimental and theoretical correlations between critical temperature and average Fermi velocity. In Sec. V we discuss the implications of the experimental correlations between T_c and v_F^* , and present our conclusions.

II. THEORETICAL MODEL

A. Band structure

In the BM model for MATBG [48], the interlayer tunneling strengths are approximated by their values at K and K'

points of the graphene Brillouin zone (BZ). This amounts to assuming the interlayer tunneling is local in the real space. To capture the particle-hole asymmetry of the flat bands predicted by *ab initio* calculations [49,50] and revealed in experimental measurements [3,4,9,22,23], nonlocal interlayer tunneling has to be taken into account in the BM model [49,51]. The resulting K -valley projected Hamiltonian is given by

$$H_0 = \begin{bmatrix} -iv_F \boldsymbol{\sigma}_{-\theta/2} \cdot \nabla_{\mathbf{r}} & T(\mathbf{r}, \mathbf{r}') \\ T^\dagger(\mathbf{r}, \mathbf{r}') & -iv_F \boldsymbol{\sigma}_{\theta/2} \cdot \nabla_{\mathbf{r}'} \end{bmatrix}, \quad (1)$$

where $\boldsymbol{\sigma}_\theta = e^{i(\theta/2)\sigma_z}(\sigma_x, \sigma_y)e^{-i(\theta/2)\sigma_z}$, $\sigma_{x,y,z}$ are Pauli matrices acting on sublattice, and $v_F \sim 10^6$ m/s is the Fermi velocity of Dirac electrons in monolayer graphene. As detailed in Appendix A, the nonlocal interlayer tunneling

$$T(\mathbf{r}, \mathbf{r}') = \sum_{n=0}^2 \sum_{\mathbf{k}} T_n(\mathbf{k}) e^{i\mathbf{q}_n \cdot \mathbf{r}} e^{i\mathbf{k} \cdot (\mathbf{r} - \mathbf{r}')}, \quad (2)$$

where the tunneling matrix $T_n(\mathbf{k})$ is wave vector dependent and can be expanded to linear order of \mathbf{k} as

$$T_n(\mathbf{k}) = T_n[1 + \xi(\hat{R}_{2n\pi/3} \mathbf{e}_{k_D}) \cdot (\mathbf{k} - \mathbf{k}_D)/k_D]. \quad (3)$$

Here $\xi = (k_\theta/t_{k_D})\partial t_k/\partial k|_{k=k_D}$ is a dimensionless coefficient characterized by the slope of interlayer tunneling amplitude t_k at Dirac point k_D , \hat{R}_ϕ denotes the two-dimensional (2D) rotation matrix with angle ϕ , and $\mathbf{e}_{k_D} = \mathbf{k}_D/k_D$ is unit vector along Γ - K direction of the graphene BZ. In the above model, the strength of nonlocal tunneling is controlled by ξ , which in turn controls the degree of asymmetry of the electron and hole flat bands [51]. The local interlayer tunneling matrix T_n is defined as

$$T_n = w_0 \sigma_0 + w_1 [\cos(2n\pi/3)\sigma_x + \sin(2n\pi/3)\sigma_y], \quad (4)$$

where w_0 and w_1 are energies of interlayer hopping between the same (AA) and different (AB) sublattices [48]. In the following calculations, we choose finite values of $\eta = w_0/w_1 < 1$ to account for the lattice relaxation effect that becomes dramatic at small twisting angles [49].

B. Hartree-Fock self-energy

The long-range Coulomb interaction is demonstrated to have a dramatic renormalization effect on the single-particle band structure of MATBG [41–43,52–54]. In this work, we mainly focus on the band renormalization of Coulomb interaction within self-consistent Hartree-Fock (HF) approximation. The Coulomb interaction is described by

$$H_{ee} = \frac{1}{2} \sum_{\alpha\alpha'} \sum_{\mathbf{q}} v_{\alpha\alpha'}(\mathbf{q}) \hat{\rho}_\alpha(\mathbf{q}) \hat{\rho}_{\alpha'}(-\mathbf{q}), \quad (5)$$

where the lumped notation $\alpha = (l\tau s\sigma)$ with l , τ , s , and σ specifying layer, valley, spin, and sublattice, $\hat{\rho}_\alpha(\mathbf{q})$ denotes electron density operator, and Coulomb potential $v_{ll'}(\mathbf{q}) = (2\pi e^2/\epsilon_q q) e^{-qd(1-\delta_{ll'})}$ with d the interlayer distance. The metallic gate screening effect is incorporated into the q -dependent dielectric constant ϵ_q (see details in Appendix C). Within HF approximation, the band structure is calculated by solving

$$\mathcal{H}(\mathbf{k}) = \mathcal{H}_0(\mathbf{k}) + \Sigma^{\text{HF}}(\mathbf{k}), \quad (6)$$

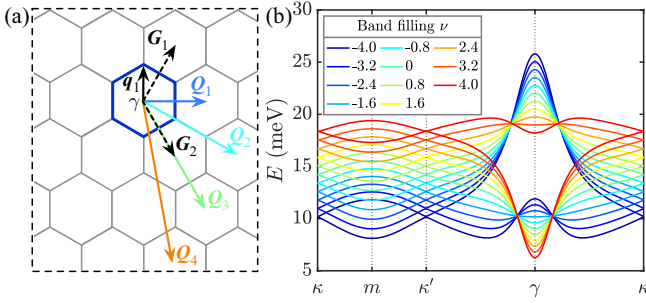


FIG. 1. (a) Schematic diagram of a moiré Brillouin zone (MBZ) and four shells of reciprocal lattice vectors. (b) Band structures of MATBG for different values of flat-band filling ν after including the HF self-energy corrections. These results are calculated by choosing twist angle $\theta = 1.05^\circ$, interlayer tunneling ratio $\eta = w_0/w_1 = 0.7$, nonlocal tunneling coefficient $\xi = 0.1$, gate-sample distance $d_s = 30$ nm, and dielectric constant $\epsilon = 25$.

where $\mathcal{H}_0(\mathbf{k})$ is the noninteracting single-particle moiré band Hamiltonian given by Eq. (1) and $\Sigma^{\text{HF}}(\mathbf{k})$ is the self-consistent HF self-energy correction (see Appendix C). The exchange interaction plays a crucial role in flavor symmetry breaking at integer flat-band fillings [41–43] and the cascade phase transitions [14,15]. For simplicity, we restrict ourselves to consider the effect of exchange interaction on band reshaping without symmetry breaking, and assume the interaction effects have a smooth dependence on the band filling. Therefore, the HF self-energy at a given band filling (Σ_v^{HF}) can be approximated by a linear interpolation between the HF self-energies calculated at the empty flat bands ($\Sigma_{\nu=-4}^{\text{HF}}$) and filled flat bands ($\Sigma_{\nu=4}^{\text{HF}}$), namely,

$$\Sigma_v^{\text{HF}} = \frac{1}{2} \left[\left(1 + \frac{\nu}{4}\right) \Sigma_{\nu=4}^{\text{HF}} + \left(1 - \frac{\nu}{4}\right) \Sigma_{\nu=-4}^{\text{HF}} \right], \quad (7)$$

where ν denotes the flat-band filling.

As a concrete example, Fig. 1(b) shows the band structures calculated by solving Eq. (6). The particle-hole asymmetric in the band structures calculated at charge neutrality $\nu = 0$ arises mainly from the nonlocal interlayer tunneling. Upon electron (hole) doping, the HF self-energy raises (lowers) the band energy around the κ and κ' points relative to the band energy around γ point of the MBZ [53]. As explained in details in Appendix C, such a behavior is the combined effects of Hartree and Fock interactions, which shift the flat bands along opposite directions and have negligible influence on bands around MBZ center where the corresponding wave-function distributions are relatively homogeneous in the real space. As illustrated in Fig. 1(b), the HF self-energy tends to flatten the flat-band bottom (top), moving the VHS to larger hole (electron) filling. All these features are consistent with earlier studies [51,53].

C. Pairing interaction

For the convenience of carrying out mean-field calculations for finite-momentum pairing states, we choose in-plane optical phonon-mediated interaction as a putative pairing mechanism because their interactions with graphene π bands are well understood [37,55,56]. Since the flat-band width

in MATBG is small compared to the optical phonon energy ($\hbar\omega_{E_2} \sim 196$ meV and $\hbar\omega_{A_1} \sim 170$ meV [55]), the phonon-mediated interaction is essentially instantaneous and competes with repulsive Coulomb interactions. The optical-phonon-mediated effective interaction that pairs electrons from opposite valleys is [37]

$$H_{ep} = -2g_\Gamma \sum_{l\tau\sigma\sigma'} \int d\mathbf{r} \psi_{l\tau\sigma\sigma}^\dagger(\mathbf{r}) \psi_{l\bar{\tau}\bar{\sigma}\sigma}^\dagger(\mathbf{r}) \psi_{l\bar{\tau}\bar{\sigma}\bar{\sigma}}(\mathbf{r}) \psi_{l\tau\sigma\bar{\sigma}}(\mathbf{r}) \\ - 2g_K \sum_{l\tau\sigma\sigma'} \int d\mathbf{r} \psi_{l\tau\sigma\sigma}^\dagger(\mathbf{r}) \psi_{l\bar{\tau}\bar{\sigma}\sigma'}^\dagger(\mathbf{r}) \psi_{l\tau\bar{\sigma}\bar{\sigma}'}(\mathbf{r}) \psi_{l\bar{\tau}\bar{\sigma}\bar{\sigma}}(\mathbf{r}), \quad (8)$$

where $\bar{\tau} = -\tau$, $\bar{s} = -s$, $\bar{\sigma} = -\sigma$, g_Γ and g_K are estimated to be 52 and 69 meV nm², denoting the electron-electron attractive strengths mediated, respectively, by optical phonons from the center (E_2) and corners (A_1/B_1) of graphene BZ.

In Sec. II B, we discussed the renormalization effect of long-range Coulomb interaction on the flat bands. For the optical-phonon-mediated electron pairing, the repulsive Coulomb interaction also plays a depairing role. In this study, we assume that the Coulomb scattering between valleys is negligible and take advantage of the repulsive intravalley Coulomb interaction as a tuning knob to control the strength of pairing interactions. Based on the above considerations, the electron-electron depairing interaction is modeled by

$$H_{ee} = \frac{u}{2} \sum_{ll'} \sum_{\tau\sigma\sigma'} \int d\mathbf{r} \rho_{l\tau\sigma\sigma}(\mathbf{r}) \rho_{l'\bar{\tau}\bar{\sigma}\bar{\sigma}'}(\mathbf{r}), \quad (9)$$

where the density operator $\rho_{l\tau\sigma\sigma}(\mathbf{r}) = \psi_{l\tau\sigma\sigma}^\dagger(\mathbf{r}) \psi_{l\tau\sigma\sigma}(\mathbf{r})$, $\psi_{l\tau\sigma\sigma}(\mathbf{r})$ is the real-space electron annihilation operator, and u is a tunable parameter. Coulomb repulsion is further assumed to have the same strength for electrons from the same and opposite valleys. We note, however, that in order to obtain superconductivity u must be reduced to values that are even smaller than what can be justified on the basis of naive screening considerations.

III. MEAN-FIELD CALCULATION

The conclusions in this paper are based on calculations of the pairing wave-vector dependence of the condensation energy for MATBG superconductors. We assume that superconducting condensation energy can be calculated using a mean-field approximation, and that the relevant Cooper pairs involve two electrons from opposite valleys. Given these assumptions, the theoretical system properties depend on the MATBG band structure model and the interaction Hamiltonian. The former is not accurately known at present, mainly because bands are renormalized by interactions [41–43], and because these renormalizations are sensitive to the three-dimensional screening environment [52–54]. For example, the Coulomb interaction tends to reduce the value η [57]. To explore the possible role of band structure renormalization, we will compare results for various band structure model parameters, and for models that account explicitly for HF self-energy corrections.

A. Self-consistent gap equation

The mean-field calculations of the finite-momentum pairing state are standard and briefly summarized in the following paragraph. The Bogoliubov–de Gennes (BdG) Hamiltonian for pairing wave vector \mathbf{q} is given by

$$\mathcal{H}_{\text{BdG}}(\mathbf{q}, \mathbf{k}) = \begin{bmatrix} \mathcal{H}(\mathbf{k}) - \mu_{\mathbf{q}} & \Delta_{\mathbf{q}}(\mathbf{k}) \\ \Delta_{\mathbf{q}}^{\dagger}(\mathbf{k}) & -\mathcal{H}^{\text{T}}(\mathbf{q} - \mathbf{k}) + \mu_{\mathbf{q}} \end{bmatrix}, \quad (10)$$

where each block acts on four-component sublattice spinors, $\Delta_{\mathbf{q}}(\mathbf{k})$ denotes pairing potential, and Σ^{HF} is incorporated in $\mathcal{H}(\mathbf{k})$ via Eq. (6). The self-consistent gap equation then reads as

$$\Delta_{\mathbf{q}}(\mathbf{k}) = \sum_{\mathbf{k}' \in \text{MBZ}} V(\mathbf{k}, \mathbf{k}') \mathcal{F}_{\mathbf{q}}(\mathbf{k}'), \quad (11)$$

where $V(\mathbf{k}, \mathbf{k}')$ is the total interaction matrix including both optical-phonon-mediated attraction and Coulomb repulsion [see Eqs. (8) and (9)], $\mathcal{F}_{\mathbf{q}}(\mathbf{k}')$ is Gorkov's anomalous Green's function [58], and the summation of \mathbf{k}' is over the MBZ. The chemical potential $\mu_{\mathbf{q}}$ is determined self-consistently by particle-number conservation.

Given a self-consistent BdG solution, the free energy of superconducting state

$$F_s(\mathbf{q}) = C_{\mathbf{q}} + An_0\mu_{\mathbf{q}} + \frac{1}{2\beta} \text{Tr} \sum_{\mathbf{k}} \ln f[-E_{\mathbf{q}}(\mathbf{k})], \quad (12)$$

where n_0 is the carrier density measured from charge neutrality, A is the sample area, $f(\epsilon)$ is the Fermi-Dirac distribution function, $E_{\mathbf{q}}(\mathbf{k})$ are the eigenvalues of the BdG Hamiltonian, and $C_{\mathbf{q}} = -\frac{1}{2} \text{Tr}(\mathcal{F}_{\mathbf{q}}^{\dagger} V \mathcal{F}_{\mathbf{q}})$ is a double-counting correction. The superconducting condensation energy is defined as $\delta F(\mathbf{q}) = F_s(\mathbf{q}) - F_n$, where F_n is the normal-state free energy calculated by Eq. (12) for zero pair potential. We use numerical results for the condensation energy as a function of \mathbf{q} , band filling ν , and model parameters to connect with experimental observables.

B. Critical magnetic field

The critical magnetic field can be extracted from mean-field calculations of the critical pairing wave vector q_c (see details in Appendix B). In the phenomenological Ginzburg-Landau theory of an isotropic superconductor, the superconducting condensation energy at finite pairing wave vector \mathbf{q} is given by

$$\delta F(\mathbf{q}) = \delta F_0 [1 - (\mathbf{q}/q_c)^2]^2, \quad (13)$$

where δF_0 is the condensation energy at $\mathbf{q} = 0$ and q_c is defined as the wave vector where $\Delta_{\mathbf{q}}$ vanishes. Our microscopic calculations are in close agreement with this expression and can be fit to determine δF_0 and q_c . As explained in Appendix B, the critical perpendicular magnetic field is related to q_c by

$$H_{c2} = \Phi_0 q_c^2 / 2\pi, \quad (14)$$

with Φ_0 the magnetic quantum flux. In addition, the supercurrent density as a function of pairing wave vector can be calculated via $\mathbf{j} = (2e/\hbar)[\partial F(\mathbf{q})/\partial \mathbf{q}]$.

IV. RESULTS

A. Bare band structure models

We first discuss results calculated with bare band structure models. Since the interaction is local, the real-space pair potential is conveniently parametrized by performing a Fourier expansion. The coefficients of reciprocal lattice vectors in this expansion are plotted as a function of pairing wave vector in the MBZ in Fig. 2(a), where the homogeneous pairing potential (\mathcal{Q}_0) exhibits a largest magnitude. In the inset of Fig. 2(a), the asymmetric behavior of $\Delta_{\mathcal{P}\mathcal{Q}_1}$ is due to rotational symmetry breaking at finite-wave-vector pairing. Figures 2(b) and 2(c) delineate the pairing-wave-vector dependence of $\delta F(\mathbf{q})$, which possesses a minimum at $q = 0$, indicating that the zero- q pairing state is the ground superconducting state. Moreover, $\delta F(\mathbf{q})$ is nearly isotropic and vanishes at a critical pairing wave vector q_c , which is small compared to the MBZ, indicating that the superconducting coherence length is many times of the moiré period.

Figures 3(a) and 3(b) show mean-field calculations of the zero- q critical temperature T_c , and the critical perpendicular magnetic field H_{c2} extracted from finite- q calculations. As expected, T_c decreases monotonously upon strengthening the repulsive Coulomb interaction between electrons. Domelike features are revealed in T_c as a function of band filling, which are reminiscent with the superconducting domes seen experimentally, but are associated here with maxima centered on the flat-band VHSs. H_{c2} possesses sharp peaks at the VHSs consistent with the phenomenological argument that H_{c2} is proportional to the effective mass of the paired electrons (see details in Appendix B). Away from the VHSs, H_{c2} decreases quickly and approaches zero when T_c becomes zero. Figure 2(c) shows the average Fermi velocity extracted from the mean-field results of T_c and H_{c2} via $v_F^* = k_B T_c / \hbar q_c$. The average velocities are 100 or more times smaller than the Dirac velocity of isolated graphene sheets $v_D \sim 10^6$ m/s, in agreement with experiment. In particular, v_F^* exhibits two prominent features: First, v_F^* is nearly independent of the pairing interaction strength and is therefore almost perfectly a pure band structure property. Second, v_F^* possesses a negative correlation with T_c characterized by V-shaped minima near the VHSs, where T_c exhibits maxima.

B. Band structure model with HF self-energy

As illustrated in Fig. 1(b), the HF self-energy correction results in band-filling-dependent band structures. We next examine the influence of HF self-energy corrections on v_F^* by performing similar mean-field calculations using the band structures given in Fig. 1(b). Figures 4(a)–4(c) show the mean-field calculations of T_c , H_{c2} , and v_F^* , respectively. As indicated in the density of states (DOS) in Fig. 4(c), the particle-hole asymmetry induced by the nonlocal interlayer tunneling is further enhanced by the interaction effect. On the hole-doping side, the VHS moves to a larger hole filling close to $\nu = -3$. If we take account of the flavor symmetry breaking near $\nu = -2$ indicated experimentally, this result is consistent with the observation [22,23] that the VHS usually appears for $\nu \in (-4, -3)$. HF band renormalization leads to multiple VHSs on the electron-doping side. The emergence

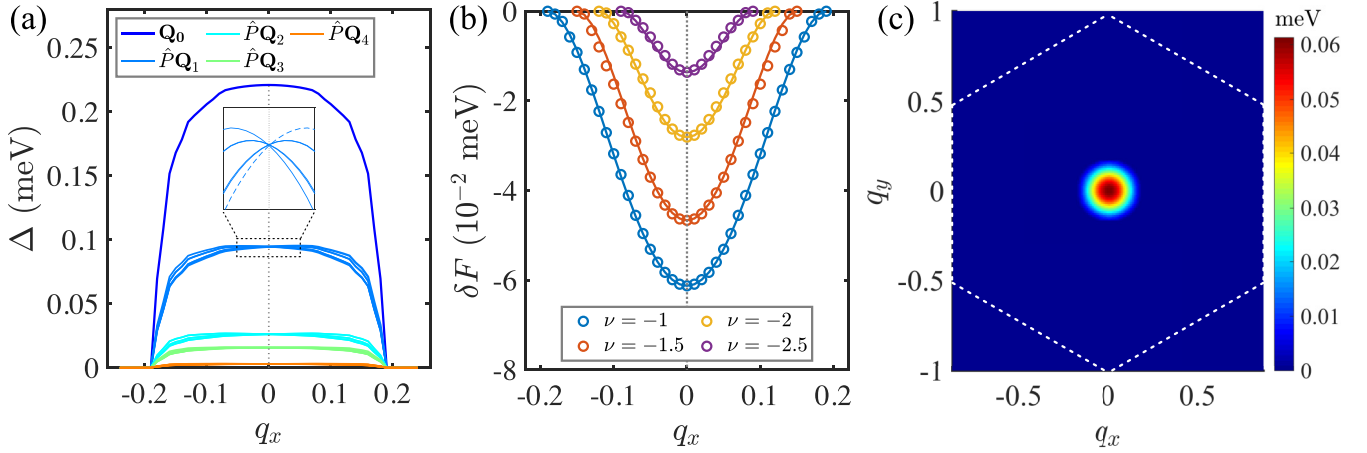


FIG. 2. Finite-wave-vector superconductivity calculated within the bare band structure model of MATBG for twisting angle $\theta = 1.07^\circ$. (a) Fourier coefficients of the real-space pairing potential expanded up to four shells of the reciprocal lattice vectors, which are generated by acting symmetry operations \hat{P} from point group C_6 on Q_i depicted in Fig. 1(a) with $Q_0 = 0$. The inset shows $\Delta_{\hat{P}Q_1}$ for flat-band filling $\nu = -1$ at small pairing wave vector q_x , where the dashed curve corresponds to Δ_{Q_1} . (b) Superconducting condensation energy normalized per moiré supercell versus q_x for different band fillings. The circles denote numerical results and solid curves are fits to Eq. (13). (c) Color scale plot of $-\delta F(\mathbf{q})$ within the MBZ (dashed hexagon) at $\nu = -1$. These results are calculated by choosing $\eta = 0.7$, $\xi = 0$, and $u = 40$ meV nm² that yields $T_c \sim 1.7$ K.

of a VHS around $\nu = 1$ may explain the property that flavor symmetry breaking appears around $\nu = 1$, but is usually absent around $\nu = -1$ [22,51]. The stronger VHS close to $\nu = 4$ is mainly caused by the Hartree potential that flattens the top of conduction band, as discussed in Sec. II B. Comparing to the results for the bare band structure model, the richer structure of the DOS for the HF model leads to richer structure for T_c and H_{c2} as functions of band fillings, as illustrated in Figs. 4(a) and 4(b). Nevertheless, as shown in Fig. 4(c), we find that the two prominent features of v_F^* revealed in the bare band structure model remain valid: (i) v_F^* is nearly independent of the pairing interaction strength; (ii) v_F^* possesses a V-shaped minimum near each VHS. Therefore, we conclude that the correlation between T_c maxima and v_F^* minima is robust.

C. Effect of Zeeman field

So far we have neglected both the possibility of flavor symmetry breaking and the role of Zeeman coupling to the electronic spin. Indeed, this assumption can be questioned since there is strong experimental evidence that the strongest superconducting dome occurs in a region of band filling where only two flavors are partially occupied and the moiré flat bands have consequently reconstructed [1–15,41–43,51]. If we were to assume that the superconducting state near $\nu = -2.3$ is spin polarized, with partially occupied valence bands for two different valleys with the same spin, the neglect of Zeeman coupling would be appropriate because pairing breaking arises from the orbit effect of applied perpendicular magnetic field. The only difference between the spin-polarized and spin-unpolarized calculations, then, would

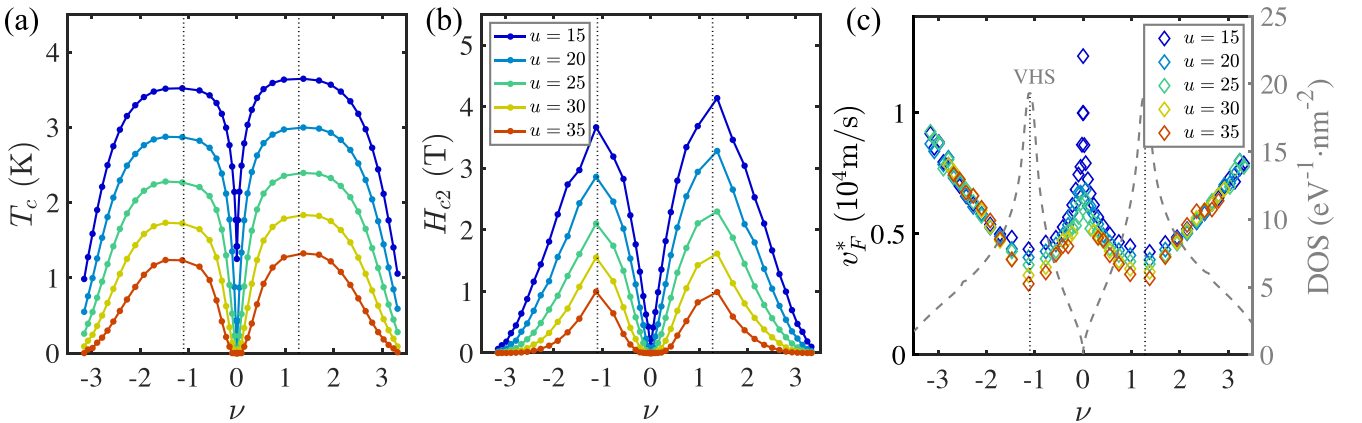


FIG. 3. (a)–(c) Zero- q critical temperature T_c , perpendicular critical magnetic field H_{c2} , and average Fermi velocity v_F^* as functions of band filling ν for several strengths of reduced Coulomb repulsion u in units of meV nm². These results are calculated for a bare MATBG band structure model with $\theta = 1.07^\circ$, $\eta = 0.7$, and $\xi = 0$ (see main text). The dotted lines indicate the values of ν at which VHSs occur, as plotted in (c). v_F^* in (c) exhibits a minimum where T_c in (a) is maximized.

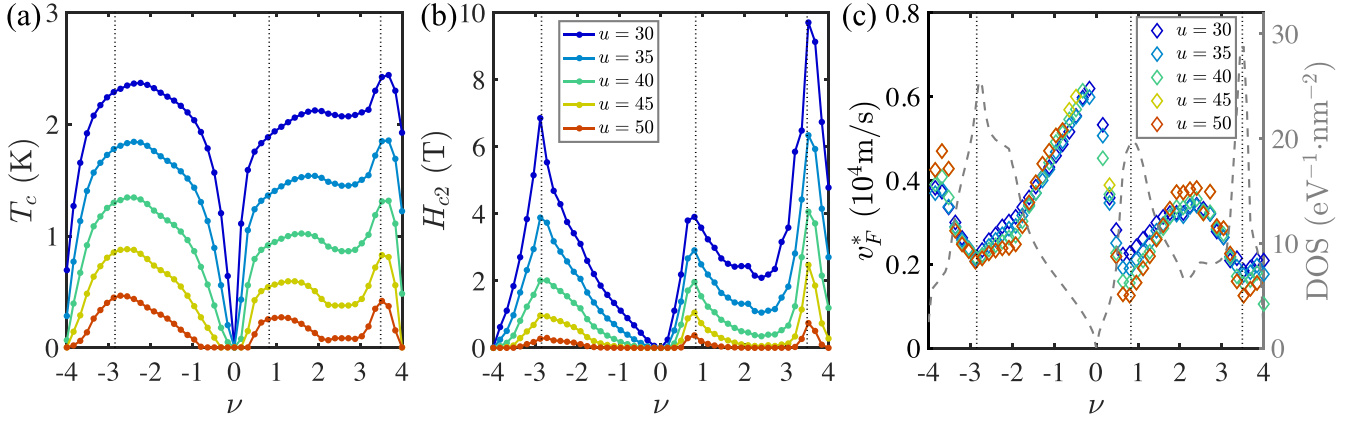


FIG. 4. (a)–(c) Zero- q critical temperature T_c , perpendicular critical magnetic field H_{c2} , and average Fermi velocity v_F^* as functions of band filling ν for several strengths of Coulomb repulsion u in units of meV nm^2 . These results are calculated for a MATBG bands that take account of HF self-energy corrections with $\theta = 1.05^\circ$, $\eta = 0.7$, and $\xi = 0.1$. The corresponding band-filling-dependent band structures are depicted in Fig. 1(b). No flavor symmetries are broken. The dotted lines indicate the values of ν at the dressed band VHSs occur. The dashed line in (c) is the dressed band DOS. v_F^* in (c) exhibits minimum versus ν near each maximum in T_c versus ν .

be a change in how the intervalley electron-phonon interactions enter the gap equation, leading simply to a change in the effective pairing interaction strength which would not alter our conclusions. On the other hand, if the superconducting state is spin singlet, the pair-breaking effect of Zeeman coupling would need to be considered. In Table I, we have listed Pauli critical fields extracted from experimental data by using $H_P \approx 1.85T_c$ (T). Since the Pauli limiting fields are much larger than H_{c2} for large T_c , experiments support the conclusion that orbital coupling is the dominant pair-breaking mechanism for perpendicular fields and justify our neglect of Zeeman effect.

Since the inclusion of HF self-energy does not change the correlation that peak values of H_{c2} occur at VHSs, we take the bare band structure model as an example to study the effect of Zeeman field on H_{c2} . As shown in Fig. 5, we compare the critical magnetic fields calculated by including only the Zeeman effect (dashed line manifesting as Pauli limit), only the orbital effect (solid line), and both effects (circles). Close to the VHS, H_P is comparable to H_{c2} because the orbital effect is suppressed due to the small Fermi velocities associated with large effective mass of the paired electrons. Away from the VHSs, however, H_P is much larger than H_{c2} , consistent with experimental observations summarized in Table I. The two peaks in H_P on the two sides of the VHS arise from Zeeman splitting of the flat bands. The critical fields calculated including both of Zeeman and orbital effects show that H_{c2} is nearly unchanged by Zeeman coupling except when the Fermi level is very close to the VHS, where H_P and H_{c2} become comparable.

D. Acoustic phonons

We have so far not explicitly included acoustic-phonon-mediated interactions, which may compete more successfully with Coulomb interactions because they are retarded. We consider the in-plane longitudinal acoustic phonons and adopt a Debye approximation for the phonon energy dispersion $\omega_q = v_{ph}|\mathbf{q}|$, where $v_{ph} = 2 \times 10^4$ m/s is the phonon velocity

in an isolated graphene sheet. We further use the deformation potential approximation and the electron-phonon coupling described by Hamiltonian

$$H_{ep} = \frac{-iD}{\sqrt{2A\rho_m}} \sum_{l,q} \sqrt{\frac{\hbar}{\omega_q}} (\mathbf{q} \cdot \hat{\mathbf{e}}_q) \rho_l(\mathbf{q}) [a_l(\mathbf{q}) + a_l^\dagger(-\mathbf{q})], \quad (15)$$

where A is the area of sample, $\hat{\mathbf{e}}_q$ is the displacement unit vector of the longitudinal phonon, $\rho_l(\mathbf{q})$ denotes the layer resolved electron density operator, $a_l(\mathbf{q})$ and $a_l^\dagger(-\mathbf{q})$ are phonon

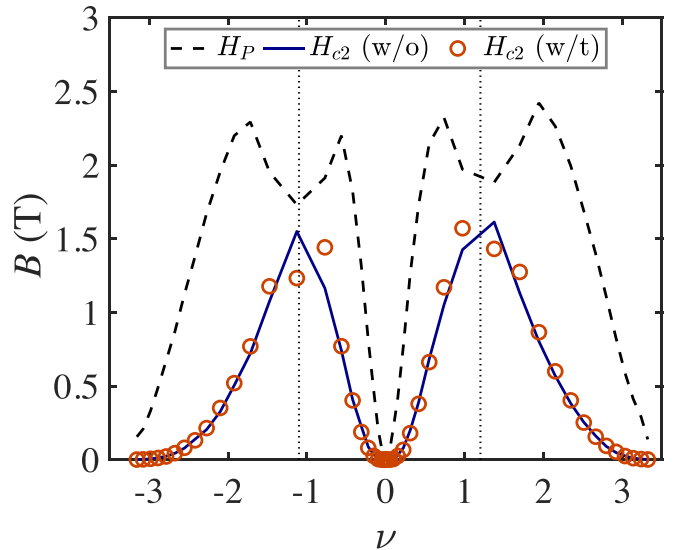


FIG. 5. Critical magnetic fields calculated at zero pairing wave vector by only including Zeeman coupling (H_P), and extracted from the critical pairing wave vector q_c with (w/t) and without (w/o) Zeeman coupling. In the presence of Zeeman coupling, $H_{c2} = (\Phi_s/2\pi)q_{x,c}q_{y,c}$, where $q_{x,c}$ and $q_{y,c}$ are the critical pairing wave vectors along x and y directions. These results are obtained by choosing $\theta = 1.07^\circ$, $\eta = 0.7$, $\xi = 0$, and $u = 30$ meV nm^2 without including the HF self-energy correction.

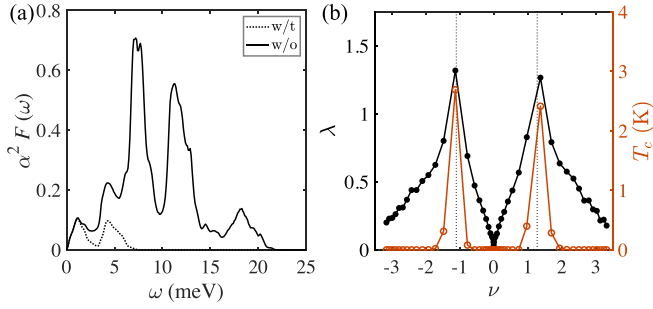


FIG. 6. (a) Fermi-surface averaged electron-acoustic phonon spectral function $\alpha^2 F(\omega)$ at the valence band VHS. The dotted and solid lines are results obtained without (w/o) umklapp processes and with (w/t) umklapp processes up to the fourth shell characterized by \mathbf{Q}_4 in Fig. 1(a). (b) Electron-acoustic phonon coupling strength λ and the estimated T_c for MATBG with $\theta = 1.07^\circ$ and $\eta = 0.7$. The dotted vertical lines in (b) show the positions of the VHSs.

annihilation and creation operators. In the following calculations, we choose the deformation potential $D = 25$ eV and the mass density of monolayer graphene $\rho_m = 7.6 \times 10^{-8}$ g/cm² [59–62].

The dimensionless electron-acoustic-phonon coupling constant

$$\lambda = 2 \int d\omega \alpha^2 F(\omega)/\omega, \quad (16)$$

where the Fermi-surface averaged electron-phonon spectrum function is defined as

$$\alpha^2 F(\omega) = \frac{1}{N_{\epsilon_F}} \sum_{nm} \sum_{\mathbf{Q}} \sum_{\mathbf{k}\mathbf{k}' \in \text{MBZ}} |g_{nm}(\mathbf{Q}; \mathbf{k}, \mathbf{k}')|^2 \times \delta(\epsilon_{nk} - \epsilon_F) \delta(\epsilon_{mk'} - \epsilon_F) \delta(\omega - \omega_{ph}). \quad (17)$$

In Eq. (17), N_{ϵ_F} denotes the Fermi-level DOS, ϵ_{nk} is the electron band energy with flat-band index n . The flat bands' projected electron-phonon coupling matrix is given by $g_{nm}(\mathbf{Q}; \mathbf{k}, \mathbf{k}')$, where the reciprocal moiré lattice vector $\mathbf{Q} \neq 0$ corresponds to umklapp electron-phonon scattering processes with phonon energy $\omega_{ph} = v_{ph}|\mathbf{k} - \mathbf{k}' - \mathbf{Q}|$. The in-plane acoustic phonon modes in the two graphene layers can be combined into symmetric and asymmetric modes. Earlier study shows that the interlayer moiré potential breaks the asymmetric phonon mode into moiré phonon minibands with gap opening at MBZ boundaries, while does not affect the linear dispersion of the symmetric phonon mode [63]. For simplification, we calculate $g_{nm}(\mathbf{Q}; \mathbf{k}, \mathbf{k}')$ in this study by directly folding the in-plane acoustic phonon mode of isolated graphene into the MBZ and ignoring the renormalization effect of moiré potential on the asymmetric phonon mode.

As illustrated in Fig. 6(a), the electron-acoustic phonon coupling is dominated by umklapp scatterings consistent with the earlier study [64]. Figure 6(b) shows the band-filling dependence of electron-phonon coupling constant λ and the superconducting critical temperatures estimated by McMillan formula $T_c = \frac{\hbar\omega_{in}}{1.2k_B} \exp[-\frac{1.04(1+\lambda)}{\lambda-\mu^*(1+0.62\lambda)}]$, where the averaged phonon frequency $\omega_{in} = \text{Coul}(2/\lambda) \int d\omega \ln(\omega) \alpha^2 F(\omega)/\omega$ [65], and the reduced Coulomb coupling strength is chosen as

$\mu^* = 0.3$ [39]. In contrast to the optical-phonon-mediated interaction, retardation does supply a formal justification for reduced Coulomb coupling [66], but since the phonon and flat-band electronic energy scales are comparable, it still does not justify the large reduction needed to match experimental T_c scales by including only the low-energy flat band of MATBG. That aside, it is clear in Fig. 6(b) that the association of T_c maxima with flat-band VHSs applies equally well to acoustic-phonon-mediated superconductivity.

In the above calculations, we choose bare band structure model as an example for the illustration of acoustic phonon-mediated superconductivity. Although the HF self-energy tends to renormalize the flat-band structures, the conclusion that T_c maxima is associated with flat-band VHSs does not change as long as the pairing is in the weak-coupling BCS regime characterized by $k_B T_c \ll \epsilon_F$.

It has been argued that the deformation potential is strongly screened by Coulomb interaction in graphene systems because the corresponding phonon mode couples to charge [67]. In contrast, the interaction between electrons and chiral combination of longitudinal and transverse acoustic phonon modes, or gauge phonons, is unscreened because gauge phonons act as pseudovector potential and couple to current instead of charge [68]. Based on the symmetry analysis of electron-acoustic phonon coupling [69], the gauge phonon-mediated electron-electron attraction possesses identical form as the electron-electron attraction [first line on the right-hand side of Eq. (8)] mediated by optical phonons around the BZ center. Since the electron-gauge phonon interaction is almost independent of band fillings, it is unlikely to alter the correlation between T_c and VHSs, and therefore the correlation between T_c maxima and v_F^* minima.

V. SUMMARY AND DISCUSSION

For a given pairing glue, weak-coupling BCS theory predicts that superconducting T_c 's are positively correlated with the DOS at Fermi level, which is determined by the Fermi-surface size and the typical quasiparticle velocity. In experiment [1,2,20] these quantities are often extracted from measurements of the frequency and temperature dependence of weak-field magnetic oscillations, which respectively measure Fermi-surface area and cyclotron effective masses. Magnetic oscillation measurements have been of limited value in MATBG because the quasiparticle masses are large and the samples are somewhat disordered. In this study we have proposed that it is possible to gain insight into superconductivity in MATBG by extracting the average Fermi velocities of the quasiparticles that participate in pairing from a combination of measured T_c and H_{c2} values.

An experimental approach to Fermi velocity estimation is needed in MATBG because quasiparticle band structures are not reliably predicted by theory. The theory problem is very challenging because (i) the cancellation effects that lead to very flat bands, also lead to extreme dependence on band structure model details and on twist angle, (ii) interactions lead to strong and filling-factor-dependent band dispersion renormalization that is imperfectly understood, and (iii) quasiparticle bands are qualitatively sensitive to flavor symmetry

breaking, also imperfectly understood, in the states from which superconductivity emerges.

In support of our proposal, we have performed mean-field calculations of the superconducting critical temperatures T_c and critical magnetic fields H_{c2} using a variety of plausible band structure and pairing models. We find that the averaged Fermi velocity defined by $\hbar v_F^* \equiv k_B T_c \sqrt{\Phi_0/2\pi H_{c2}}$ is nearly independent of the pairing interaction, verifying that it is almost entirely a property of the quasiparticles present at the Fermi level. For a fixed pairing glue model we find that v_F^* is always negatively correlated with T_c and that it has a V-shaped cusp when the Fermi level is placed at the flat-band VHS. By varying different types of model parameters (Sec. IV and Appendix D), we find that such a T_c - v_F^* correlation is independent of the details of band structure, which is sensitive to electrostatic doping, twisting angle [48], strain [21,49], substrate environment [17,22,23]. Since the experimental values of v_F^* , summarized in Table I, do not show any indication of a such correlation between v_F^* and T_c as the band filling is varied, we conclude that it is the pairing glue that is mainly responsible for the shape and position of the superconducting domes. The dependence of the pairing glue on band-filling factor is likely due to short-range spin and/or valley order fluctuations that are optimized for superconductivity near the peaks of the experimental superconducting domes [40]. A number of interesting possibilities for these fluctuations have already been proposed theoretically, including ferromagnetic fluctuations in systems with interaction-enhanced intervalley scattering [36,40,53,70,71] and skyrmion-mediated pairing [18] in systems with enhanced intervalley coherence.

ACKNOWLEDGMENTS

The authors acknowledge helpful discussions with Chunli Huang, Eslam Khalaf, Andrea Young, Ming Xie, and Tobias Wolf. This work was supported by the U.S. Department of Energy, Office of Science, Basic Energy Sciences, under Award No. DESC0022106. Numerical calculations were performed using supercomputing resources at the Texas Advanced Computing Center (TACC).

APPENDIX A: NONLOCAL INTERLAYER TUNNELING MODEL

Here we rederive the BM model of MATBG by including the momentum dependence of the interlayer tunneling matrix, which takes the following form:

$$\begin{aligned} [T_{pk}]_{\sigma'\sigma} &= \frac{1}{N} \sum_{\mathbf{R}\mathbf{R}'} t_{\sigma'\sigma}(\mathbf{R} + \boldsymbol{\tau}_\sigma - \mathbf{R}' - \boldsymbol{\tau}'_{\sigma'}) \\ &\quad \times e^{i\mathbf{k}\cdot(\mathbf{R}+\boldsymbol{\tau}_\sigma) - i\mathbf{p}\cdot(\mathbf{R}'+\boldsymbol{\tau}'_{\sigma'})} \\ &= \frac{1}{\Omega} \sum_{\mathbf{g}_1\mathbf{g}_2} t_{\sigma'\sigma}(\mathbf{k} - \mathbf{g}_1) \delta_{\mathbf{k}-\mathbf{g}_1, \mathbf{p}-\mathbf{g}_2} e^{i(\mathbf{g}_1\cdot\boldsymbol{\tau}_\sigma - \mathbf{g}_2\cdot\boldsymbol{\tau}'_{\sigma'})}, \quad (\text{A1}) \end{aligned}$$

where $\sigma = A, B$ are sublattice indices, \mathbf{k} and \mathbf{p} are wave vectors measured from the center of the graphene BZ, \mathbf{R} are the real-space positions of the graphene unit cells, $\boldsymbol{\tau}_\sigma$ denotes the sublattice position within a unit cell, the area of which is

$\Omega = \sqrt{3}a_0^2/2$ with graphene lattice constant $a_0 = 2.46 \text{ \AA}$, and $\mathbf{g}_{1,2}$ are graphene reciprocal lattice vectors. In Eq. (A1), labels with (without) primes are defined in the top (bottom) graphene layer in MATBG. By keeping the dominant contribution of the Fourier coefficient of the interlayer tunneling, we have

$$\begin{aligned} [T_{pk}]_{\sigma'\sigma} &= \frac{1}{\Omega} \sum_{j=0}^2 t_{\sigma'\sigma}(\hat{\mathbf{R}}_{2j\pi/3} \mathbf{k}_D + \delta\mathbf{k}) \\ &\quad \times \delta_{\mathbf{k}, \mathbf{p} + \hat{\mathbf{R}}_{2j\pi/3} \mathbf{k}_D} e^{i(\mathbf{k}_D - \hat{\mathbf{R}}_{2j\pi/3} \mathbf{k}_D) \cdot (\boldsymbol{\tau}_\sigma - \boldsymbol{\tau}'_{\sigma'})}, \quad (\text{A2}) \end{aligned}$$

where \mathbf{k}_D is the wave vector of K point of the BZ of the bottom layer graphene, $\delta\mathbf{k}$ is measured from K point, and the 2D rotational operator is defined as

$$\hat{\mathbf{R}}_\theta = \begin{pmatrix} \cos \theta & -\sin \theta \\ \sin \theta & \cos \theta \end{pmatrix}. \quad (\text{A3})$$

In the original BM model, $t_{\sigma'\sigma}(\hat{\mathbf{R}}_{2j\pi/3} \mathbf{k}_D + \delta\mathbf{k}) \approx t_{\sigma'\sigma}(\hat{\mathbf{R}}_{2j\pi/3} \mathbf{k}_D) = t_{\sigma'\sigma}(k_D)$ due to C_3 symmetry. By keeping the momentum dependence of $t_{\sigma'\sigma}$ up to linear term,

$$\begin{aligned} t_{\sigma'\sigma}(\hat{\mathbf{R}}_{2j\pi/3} \mathbf{k}_D + \delta\mathbf{k}) &= t_{\sigma'\sigma}(k_D) + (\hat{\mathbf{R}}_{2j\pi/3} \mathbf{e}_{k_D}) \cdot (\mathbf{k} - \mathbf{k}_D) \\ &\quad \times (\partial t_{\sigma'\sigma} / \partial k)|_{k=k_D}, \quad (\text{A4}) \end{aligned}$$

where $\mathbf{e}_{k_D} = \mathbf{k}_D/k_D$ is a unit vector along Γ - K direction within graphene BZ. For simplification, we define a dimensionless parameter $\xi = (k_D/t_{\sigma'\sigma})(\partial t_{\sigma'\sigma}/\partial k)|_{k=k_D}$. Therefore, the interlayer tunneling can be organized as Eq. (3), where the hopping energies are given by $w_0 = \Omega^{-1}t_{AA}(k_D)$ and $w_1 = \Omega^{-1}t_{AB}(k_D)$.

APPENDIX B: GINZBURG-LANDAU THEORY OF SUPERCONDUCTIVITY

The Ginzburg-Landau (GL) theory of superconductivity is based on the expansion of free energy of a system in powers of superconducting order parameter [72]. In the presence of magnetic field, the free energy

$$\begin{aligned} F_s &= F_n + \int d\mathbf{r} \left[\frac{\hbar^2}{2m^*} \left| \left(\nabla - i \frac{2e}{\hbar c} \mathbf{A} \right) \psi \right|^2 + \alpha(T) |\psi|^2 \right. \\ &\quad \left. + \frac{\beta(T)}{2} |\psi|^4 + \frac{\mathbf{B}^2}{8\pi} \right], \quad (\text{B1}) \end{aligned}$$

where $\psi = \sqrt{n_s} e^{i\phi}$ is the complex order parameter, ϕ is the phase of order parameter, n_s , m^* , and $2e$ are the density, effective mass, and total charge of electron pair. By varying the GL free energy with respect to magnetic vector potential \mathbf{A} and order parameter ψ^* , the supercurrent density

$$\mathbf{j} = \frac{2\hbar n_s}{m^*} \left(\nabla \phi - \frac{2e}{\hbar c} \mathbf{A} \right), \quad (\text{B2})$$

and the GL equation

$$\frac{1}{2m^*} \left(-i\hbar \nabla - \frac{2e}{c} \mathbf{A} \right)^2 \psi + \alpha(T) \psi + \beta(T) |\psi|^2 \psi = 0. \quad (\text{B3})$$

The GL coherence length or magnetic length ℓ_c is defined as

$$\ell_c = \sqrt{\hbar^2/2m^*|\alpha|}. \quad (\text{B4})$$

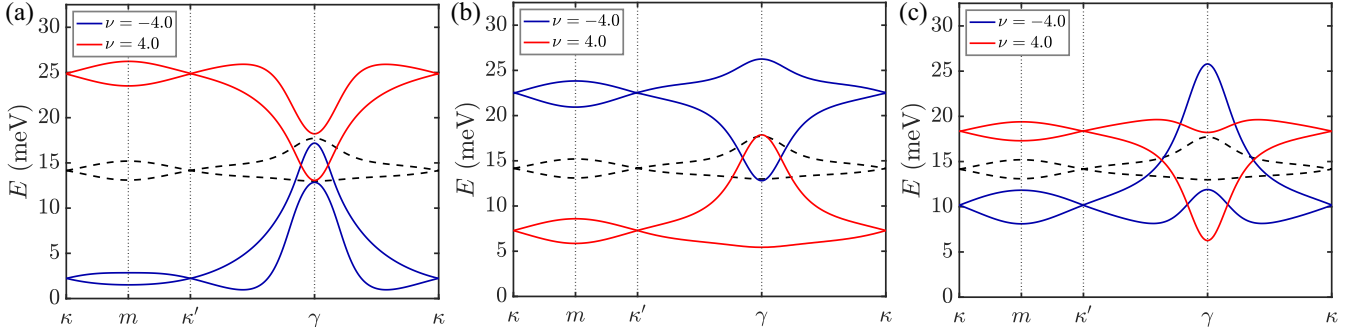


FIG. 7. The effects of (a) Hartree, (b) Fock, and (c) Hartree-Fock self-energies on the flat bands of MATBG with $\theta = 1.05^\circ$ at band filling $\nu = \pm 4$. The dashed curves show the noninteracting flat bands, where the particle-hole asymmetry is attributed to the nonlocal interlayer tunneling described by Eq. (3). These calculations are performed by choosing $\eta = 0.7$, $\xi = 0.1$, $d_s = 30$ nm, and the effective dielectric constant $\epsilon = 25$.

The upper critical magnetic field H_{c2} of type-II superconductor can be estimated from Eq. (B3). When the externally applied magnetic field is close to H_{c2} , the superconducting order parameter ψ becomes small, and Eq. (B3) can be linearized into

$$\frac{1}{2m^*} \left(-i\hbar\nabla - \frac{2e}{c}\mathbf{A} \right)^2 \psi + \alpha\psi = 0, \quad (\text{B5})$$

which resembles the Schrödinger equation for a particle with mass m^* and charge $2e$ subject to magnetic field $\mathbf{B} = \nabla \times \mathbf{A}$. The solution of Eq. (B5) is Landau levels with $|\alpha| = \hbar\omega_c(n + 1/2)$, where n are positive integers and $\omega_c = 2eB/m^*c$ is the cyclotron frequency. Upper critical magnetic field H_{c2} is defined as the maximum magnetic field that validates the solution, thus,

$$H_{c2} = m^*c|\alpha|/\hbar e = \frac{\Phi_0}{2\pi\ell_c^2}, \quad (\text{B6})$$

where $\Phi_0 = \pi\hbar c/e \approx 2.067 \times 10^{-15}$ T m² is the magnetic (superconducting) quantum flux.

We next show that ℓ_c and H_{c2} can be extracted from the free energy for finite-momentum pairing superconducting state. For pairing wave vector \mathbf{q} , the real-space order parameter can be written as $\psi = \sqrt{n_s(\mathbf{q})}e^{i\mathbf{q}\cdot\mathbf{r}}$. In the absence of external magnetic field, the superconducting condensation energy is reduced to

$$\delta F(\mathbf{q}) = \frac{\hbar^2\mathbf{q}^2}{2m^*}n_s(\mathbf{q}) + \alpha n_s(\mathbf{q}) + \frac{1}{2}\beta n_s^2(\mathbf{q}), \quad (\text{B7})$$

and Eq. (B3) reduces to

$$\frac{\hbar^2\mathbf{q}^2}{2m^*} + \alpha + \beta n_s(\mathbf{q}) = 0. \quad (\text{B8})$$

Therefore, we have

$$\delta F(\mathbf{q}) = -\frac{1}{2\beta} \left(|\alpha| - \frac{\hbar^2\mathbf{q}^2}{2m^*} \right)^2 = \delta F(0)[1 - (\mathbf{q}/q_c)^2]^2, \quad (\text{B9})$$

where $q_c = \sqrt{2m^*|\alpha|/\hbar^2} = 1/\ell_c$ is the critical pairing wave vector defined by $\delta F(q_c) = 0$. Equations (B4) and (B6) lead to

$$H_{c2} = \Phi_0 q_c^2 / 2\pi. \quad (\text{B10})$$

The supercurrent density of Eq. (B2) is reduced to

$$\mathbf{j} = 2\hbar e n_s(\mathbf{q})\mathbf{q}/m^* = 2e n_s(\mathbf{q})\mathbf{v}, \quad (\text{B11})$$

where $\mathbf{v} = \hbar\mathbf{q}/m^*$ is the velocity of Cooper pair. In this work, we calculate the free energy as a function of pairing wave vector within mean-field theory. By employing the relation given in Eq. (B7), we have the supercurrent density

$$\mathbf{j} = (2e/\hbar)\partial F(\mathbf{q})/\partial\mathbf{q}. \quad (\text{B12})$$

In the above derivations, α and β are assumed to be independent of pairing wave vector \mathbf{q} . Such an assumption in MATBG can be justified by Fig. 2(b), where our numerical calculations of $\delta F(\mathbf{q})$ can be well fitted by Eq. (B9).

APPENDIX C: SELF-CONSISTENT HARTREE-FOCK CALCULATIONS

The effects of Coulomb interaction on superconductivity comprise of two aspects, renormalizing single-particle band structure and breaking Cooper pair. Since the energy scale of band renormalization is much larger than that of superconducting order parameter, the two effects may be treated independently. In this section, we focus the band renormalization within the self-consistent HF approximation. For MATBG, the Coulomb interaction can be organized as

$$\begin{aligned} H_{ee} = & \frac{1}{2} \sum_{\alpha\beta} \sum_{nmn'm'} \sum_{\mathbf{k}\mathbf{k}'\mathbf{k}_1} v_{\alpha\beta}(\mathbf{k}' - \mathbf{k} + \mathbf{G}_{n'} - \mathbf{G}_n) \\ & \times \psi_{n'\alpha}^\dagger(\mathbf{k}') \psi_{m'\beta}^\dagger(\mathbf{k}_1) \psi_{m\beta}(\mathbf{k}_1) \psi_{n\alpha}(\mathbf{k}) \\ & \times \delta_{\mathbf{k}' - \mathbf{k} + \mathbf{G}_{n'} - \mathbf{G}_n, \mathbf{k}_1 - \mathbf{k}_1 + \mathbf{G}_m - \mathbf{G}_m}, \end{aligned} \quad (\text{C1})$$

where the summation of wave vectors are over MBZ, the lumped notation $\alpha = (l\tau s\sigma)$ with l , τ , s , and σ specifying layer, valley, spin, and sublattice, and n, m, n', m' label moiré reciprocal lattice vectors. The Coulomb potential

$$v_{\alpha\beta}(\mathbf{q}) = \frac{2\pi e^2}{\epsilon_0(\mathbf{q})q} e^{-qd(1-\delta_{l'l'})}, \quad (\text{C2})$$

which is assumed to be independent of valley, spin, and sublattice. Here ϵ_0 is the vacuum permittivity, d is the inter-layer distance, and the dielectric function $\epsilon(\mathbf{q})$ captures the

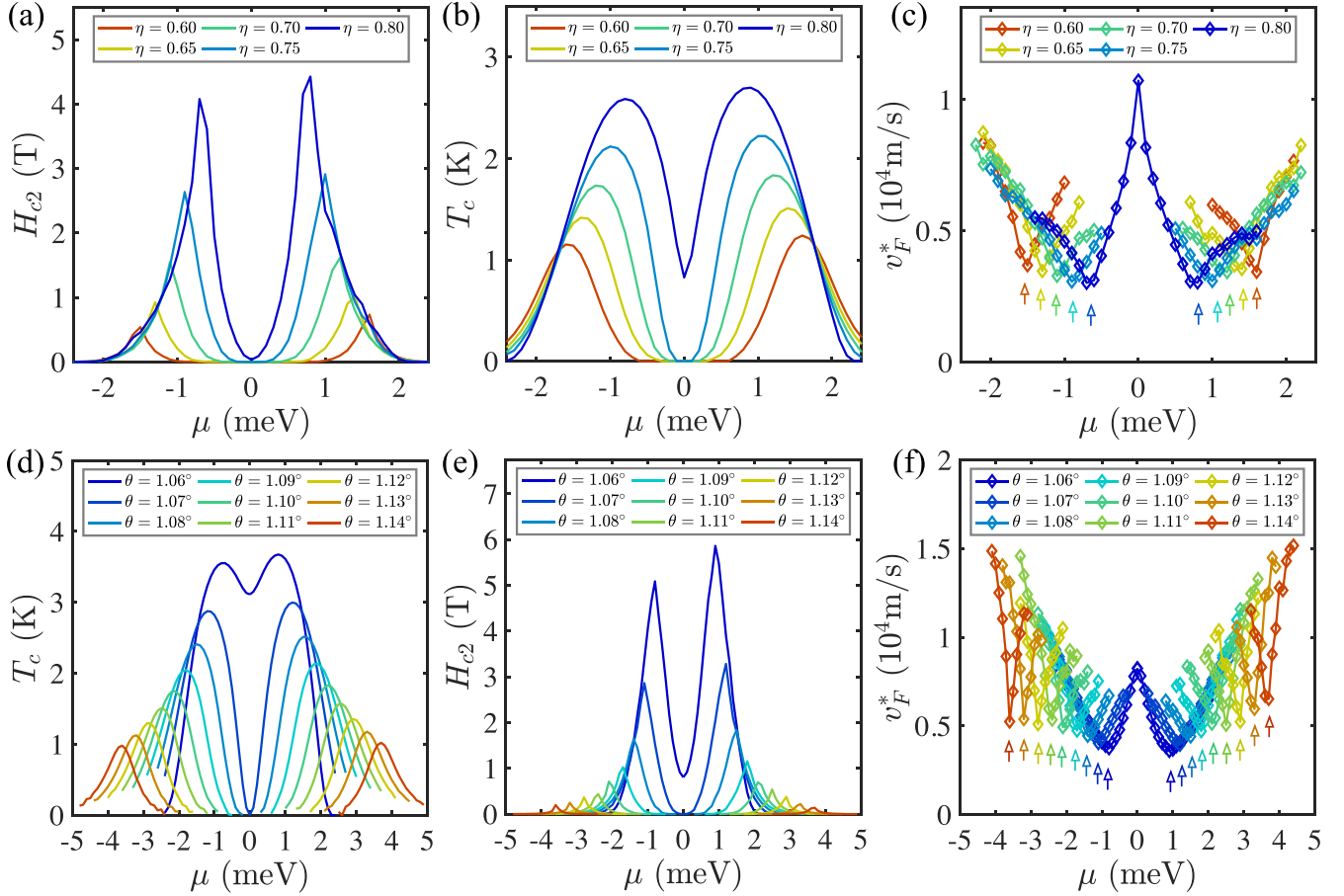


FIG. 8. (a)–(c) T_c , H_{c2} , and v_F^* as functions of chemical potential μ measured from charge neutrality for each value of η . In these calculations, we choose $\theta = 1.07^\circ$ and $u = 30 \text{ meV nm}^2$. (d)–(f) T_c , H_{c2} , and v_F^* as functions of μ for several different twist angles. In these calculations, we choose $\eta = 0.7$ and $u = 20 \text{ meV nm}^2$. Vertical arrows in (c) and (f) highlight the positions of flat-band VHSs.

screening effects, including the external and internal screening as detailed below.

For external environment screening, we consider the MATBG sample sandwiched by hexagonal boron nitride (h-BN) with a typical thickness of d_s terminated by dual metallic gates. Therefore, the screened Coulomb potential in the MATBG layer can be obtained by solving the following Poisson's equation:

$$\nabla \cdot [\epsilon(\mathbf{r}) \nabla \Phi(\mathbf{r})] = -4\pi e \delta(z), \quad (\text{C3})$$

where the permittivity $\epsilon(\mathbf{r})$ takes a general matrix form. In this study, we approximate $\epsilon(\mathbf{r}) = \text{diag}(\epsilon_{\parallel}, \epsilon_{\parallel}, \epsilon_{\perp})$ with $\epsilon_{\parallel} \approx 6.9$ and $\epsilon_{\perp} \approx 3.48$ being the in-plane and perpendicular permittivity of h-BN [73]. By solving Eq. (C3),

$$\frac{1}{\epsilon_{\text{en}}} = \frac{1}{\sqrt{\epsilon_{\parallel} \epsilon_{\perp}}} \tanh(\sqrt{\epsilon_{\parallel} / \epsilon_{\perp}} q d_s), \quad (\text{C4})$$

where anisotropic permittivity of h-BN leads to a reduction on the Coulomb potential in the sandwiched MATBG layer.

For the internal screening, random-phase calculations show that the static dielectric function possesses a nontrivial momentum structure and is strongly enhanced near magic twisting angle [74,75], where the active bands become extremely flat. For simplification, in this study, we adopt a constant dielectric function to mimic the effect of internal

screening. Therefore, the Coulomb potential takes the following form:

$$v_{\alpha\beta}(\mathbf{q}) = \frac{2\pi e^2}{\epsilon_0 \tilde{\epsilon} q} e^{-q d (1 - \delta_{\mu'})} \tanh\left(\sqrt{\frac{\epsilon_{\parallel}}{\epsilon_{\perp}}} q d_s\right), \quad (\text{C5})$$

where the constant $\tilde{\epsilon}$ contains contributions from $\sqrt{\epsilon_{\parallel} \epsilon_{\perp}}$ and the internal static screening effect.

Based on the above screened interaction model, the Hartree self-energy

$$\Sigma_{n\alpha, m\alpha}^H(\mathbf{k}) = \frac{1}{A} \sum_{n'\alpha', \mathbf{k}'} v_{\alpha\alpha'}(\mathbf{G}_n - \mathbf{G}_m) [\rho(\mathbf{k}')]_{m'\alpha', n'\alpha'}, \quad (\text{C6})$$

where $\rho(\mathbf{k})$ is the density operator and $m' = n + n' - m$. The Hartree self-energy $\Sigma_{n\alpha, m\alpha}^H$ is independent of the moiré wave vector \mathbf{k} , and is diagonal in the layer, valley, spin, and sublattice subspaces. The Fock self-energy

$$\begin{aligned} \Sigma_{n\alpha, m\beta}^F(\mathbf{k}) &= -\frac{1}{A} \sum_{n'\mathbf{k}'} v_{\alpha\beta}(\mathbf{k} - \mathbf{k}' + \mathbf{G}_n - \mathbf{G}_{n'}) \\ &\quad \times [\rho(\mathbf{k}')]_{n'\alpha', (n'+m-n)\beta}, \end{aligned} \quad (\text{C7})$$

where the minus sign stems from exchange of fermions. The Hartree-type energy correction

$$E_c^H = -\frac{1}{2} \text{Tr}[\rho \Sigma^H], \quad (\text{C8})$$

where $\rho = \sum_{\mathbf{k}} \rho(\mathbf{k})$. The Fock-type energy correction

$$E_c^F = -\frac{1}{2} \sum_{\mathbf{k}} \text{Tr}[\rho(\mathbf{k})\Sigma^F(\mathbf{k})]. \quad (\text{C9})$$

The total mean-field energy correction

$$E_c = E_c^H + E_c^F = -\frac{1}{2} \sum_{\mathbf{k}} \text{Tr}[\rho(\mathbf{k})\Sigma(\mathbf{k})], \quad (\text{C10})$$

where $\Sigma(\mathbf{k}) = \Sigma^H + \Sigma^F(\mathbf{k})$ is the HF self-energy. In the numerical calculations, we choose the isolated bilayer graphene with a relative rotation angle equaling to that of MATBG as a reference system, and replace the density operator $\rho(\mathbf{k})$ appeared in the above equations by

$$\delta\rho(\mathbf{k}) = \rho(\mathbf{k}) - \rho_0(\mathbf{k}), \quad (\text{C11})$$

with $\rho_0(\mathbf{k})$ the density operator of the reference system.

Figure 7 shows the effects of HF self-energy on the single-particle band structure of MATBG. The results for $\nu = \pm 4$ are obtained by solving Eqs. (C6) and (C7) self-consistently until convergences are reached. As illustrated in Fig. 7(a), the Hartree self-energy tends to shift the flat bands near MBZ corners to lower (higher) energies upon emptying (filling) the flat bands. The bands around γ point are almost unchanged. In contrast, the Fock self-energy tends to influence the band structure in an opposite way as illustrated in Fig. 7(b). The synergistic effects of Hartree and Fock self-energies on band structure are shown in Fig. 7(c), where the band edges become

flatter comparing to the noninteracting single-particle bands. The linear interpolations of the results shown in Fig. 7(c) are given in Fig. 1(b).

APPENDIX D: OTHER MODEL PARAMETERS

To further explore the correlation between T_c and v_F^* , we perform similar mean-field calculations by varying twisting angle (θ) and interlayer tunneling ratio (η). In Sec. IV B, we show that the inclusion of HF self-energy in the band structure model does not alter the correlation between T_c and v_F^* . In order to facilitate the numerical calculations, here we calculate T_c and v_F^* within the bare band structure model by varying η and θ . We note that, in order to indicate the changes of the flat-band width, T_c , H_{c2} , and v_F^* are plotted versus chemical potential μ instead of band-filling factor. Over the illustrated parameter range studied in Fig. 8, the flat-band width is larger at smaller η and larger θ . Accordingly, decreasing η or increasing θ tends to reduce T_c as shown in Figs. 8(a) and 8(d), where domelike features in T_c are peaked around the shifting VHSs. As illustrated in Figs. 8(b) and 8(e), sharp peaks of H_{c2} are also found at VHSs, and the magnitude of H_{c2} is dramatically suppressed for models with larger flat-band width. The extracted v_F^* are plotted in Figs. 8(c) and 8(f), and are as expected larger for larger flat-band widths. For every band structure model, v_F^* possesses a V-shaped minimum near each VHS, which is always coincident with the maximum of T_c . Overall, these results further demonstrate that the correlation between T_c maxima and v_F^* minima are robust.

-
- [1] Y. Cao, V. Fatemi, S. Fang, K. Watanabe, T. Taniguchi, E. Kaxiras, and P. Jarillo-Herrero, Unconventional superconductivity in magic-angle graphene superlattices, *Nature (London)* **556**, 43 (2018).
- [2] Y. Cao, V. Fatemi, A. Demir, S. Fang, S. L. Tomarken, J. Y. Luo, J. D. Sanchez-Yamagishi, K. Watanabe, T. Taniguchi, E. Kaxiras, R. C. Ashoori, and P. Jarillo-Herrero, Correlated insulator behaviour at half-filling in magic-angle graphene superlattices, *Nature (London)* **556**, 80 (2018).
- [3] M. Yankowitz, S. Chen, H. Polshyn, Y. Zhang, K. Watanabe, T. Taniguchi, D. Graf, A. F. Young, and C. R. Dean, Tuning superconductivity in twisted bilayer graphene, *Science* **363**, 1059 (2019).
- [4] Y. Xie, B. Lian, B. Jäck, X. Liu, C.-L. Chiu, K. Watanabe, T. Taniguchi, B. A. Bernevig, and A. Yazdani, Spectroscopic signatures of many-body correlations in magic-angle twisted bilayer graphene, *Nature (London)* **572**, 101 (2019).
- [5] A. Kerelsky, L. J. McGilly, D. M. Kennes, L. Xian, M. Yankowitz, S. Chen, K. Watanabe, T. Taniguchi, J. Hone, C. Dean, A. Rubio, and A. N. Pasupathy, Maximized electron interactions at the magic angle in twisted bilayer graphene, *Nature (London)* **572**, 95 (2019).
- [6] Y. Choi, J. Kemmer, Y. Peng, A. Thomson, H. Arora, R. Polski, Y. Zhang, H. Ren, J. Alicea, G. Refael, F. von Oppen, K. Watanabe, T. Taniguchi, and S. Nadj-Perge, Electronic correlations in twisted bilayer graphene near the magic angle, *Nat. Phys.* **15**, 1174 (2019).
- [7] Y. Jiang, X. Lai, K. Watanabe, T. Taniguchi, K. Haule, J. Mao, and E. Y. Andrei, Charge order and broken rotational symmetry in magic-angle twisted bilayer graphene, *Nature (London)* **573**, 91 (2019).
- [8] A. L. Sharpe, E. J. Fox, A. W. Barnard, J. Finney, K. Watanabe, T. Taniguchi, M. A. Kastner, and D. Goldhaber-Gordon, Emergent ferromagnetism near three-quarters filling in twisted bilayer graphene, *Science* **365**, 605 (2019).
- [9] X. Lu, P. Stepanov, W. Yang, M. Xie, M. A. Aamir, I. Das, C. Urgell, K. Watanabe, T. Taniguchi, G. Zhang, A. Bachtold, A. H. MacDonald, and D. K. Efetov, Superconductors, orbital magnets and correlated states in magic-angle bilayer graphene, *Nature (London)* **574**, 653 (2019).
- [10] X. Hu, T. Hyart, D. I. Pikulin, and E. Rossi, Geometric and Conventional Contribution to the Superfluid Weight in Twisted Bilayer Graphene, *Phys. Rev. Lett.* **123**, 237002 (2019).
- [11] M. Serlin, C. L. Tschirhart, H. Polshyn, Y. Zhang, J. Zhu, K. Watanabe, T. Taniguchi, L. Balents, and A. F. Young, Intrinsic quantized anomalous Hall effect in a moiré heterostructure, *Science* **367**, 900 (2020).
- [12] A. Julku, T. J. Peltonen, L. Liang, T. T. Heikkilä, and P. Törmä, Superfluid weight and Berezinskii-Kosterlitz-Thouless transition temperature of twisted bilayer graphene, *Phys. Rev. B* **101**, 060505(R) (2020).
- [13] F. Xie, Z. Song, B. Lian, and B. A. Bernevig, Topology-Bounded Superfluid Weight in Twisted Bilayer Graphene, *Phys. Rev. Lett.* **124**, 167002 (2020).

- [14] D. Wong, K. P. Nuckolls, M. Oh, B. Lian, Y. Xie, S. Jeon, K. Watanabe, T. Taniguchi, B. A. Bernevig, and A. Yazdani, Cascade of electronic transitions in magic-angle twisted bilayer graphene, *Nature (London)* **582**, 198 (2020).
- [15] U. Zondiner, A. Rozen, D. Rodan-Legrain, Y. Cao, R. Queiroz, T. Taniguchi, K. Watanabe, Y. Oreg, F. von Oppen, A. Stern, E. Berg, P. Jarillo-Herrero, and S. Ilani, Cascade of phase transitions and Dirac revivals in magic-angle graphene, *Nature (London)* **582**, 203 (2020).
- [16] L. Balents, C. R. Dean, D. K. Efetov, and A. F. Young, Superconductivity and strong correlations in moiré flat bands, *Nat. Phys.* **16**, 725 (2020).
- [17] M. Oh, K. P. Nuckolls, D. Wong, R. L. Lee, X. Liu, K. Watanabe, T. Taniguchi, and A. Yazdani, Evidence for unconventional superconductivity in twisted bilayer graphene, *Nature (London)* **600**, 240 (2021).
- [18] E. Khalaf, S. Chatterjee, N. Bultinck, M. P. Zaletel, and A. Vishwanath, Charged skyrmions and topological origin of superconductivity in magic-angle graphene, *Sci. Adv.* **7**, eabf5299 (2021).
- [19] P. Stepanov, M. Xie, T. Taniguchi, K. Watanabe, X. Lu, A. H. MacDonald, B. A. Bernevig, and D. K. Efetov, Competing Zero-Field Chern Insulators in Superconducting Twisted Bilayer Graphene, *Phys. Rev. Lett.* **127**, 197701 (2021).
- [20] J. M. Park, Y. Cao, K. Watanabe, T. Taniguchi, and P. Jarillo-Herrero, Tunable strongly coupled superconductivity in magic-angle twisted trilayer graphene, *Nature (London)* **590**, 249 (2021).
- [21] S. Carr, S. Fang, P. Jarillo-Herrero, and E. Kaxiras, Pressure dependence of the magic twist angle in graphene superlattices, *Phys. Rev. B* **98**, 085144 (2018).
- [22] P. Stepanov, I. Das, X. Lu, A. Fahimniya, K. Watanabe, T. Taniguchi, F. H. L. Koppens, J. Lischner, L. Levitov, and D. K. Efetov, Untying the insulating and superconducting orders in magic-angle graphene, *Nature (London)* **583**, 375 (2020).
- [23] Y. Saito, J. Ge, K. Watanabe, T. Taniguchi, and A. F. Young, Independent superconductors and correlated insulators in twisted bilayer graphene, *Nat. Phys.* **16**, 926 (2020).
- [24] X. Liu, Z. Wang, K. Watanabe, T. Taniguchi, O. Vafek, and J. I. A. Li, Tuning electron correlation in magic-angle twisted bilayer graphene using coulomb screening, *Science* **371**, 1261 (2021).
- [25] H. Guo, X. Zhu, S. Feng, and R. T. Scalettar, Pairing symmetry of interacting fermions on a twisted bilayer graphene superlattice, *Phys. Rev. B* **97**, 235453 (2018).
- [26] J. F. Dodaro, S. A. Kivelson, Y. Schattner, X. Q. Sun, and C. Wang, Phases of a phenomenological model of twisted bilayer graphene, *Phys. Rev. B* **98**, 075154 (2018).
- [27] C.-C. Liu, L.-D. Zhang, W.-Q. Chen, and F. Yang, Chiral Spin Density Wave and $d + id$ Superconductivity in the Magic-Angle-Twisted Bilayer Graphene, *Phys. Rev. Lett.* **121**, 217001 (2018).
- [28] H. Isobe, N. F. Q. Yuan, and L. Fu, Unconventional Superconductivity and Density Waves in Twisted Bilayer Graphene, *Phys. Rev. X* **8**, 041041 (2018).
- [29] M. Fidrysiak, M. Zegrodnik, and J. Spałek, Unconventional topological superconductivity and phase diagram for an effective two-orbital model as applied to twisted bilayer graphene, *Phys. Rev. B* **98**, 085436 (2018).
- [30] D. M. Kennes, J. Lischner, and C. Karrasch, Strong correlations and $d + id$ superconductivity in twisted bilayer graphene, *Phys. Rev. B* **98**, 241407(R) (2018).
- [31] Y. Sherkunov and J. J. Betouras, Electronic phases in twisted bilayer graphene at magic angles as a result of Van Hove singularities and interactions, *Phys. Rev. B* **98**, 205151 (2018).
- [32] J. González and T. Stauber, Kohn-Luttinger Superconductivity in Twisted Bilayer Graphene, *Phys. Rev. Lett.* **122**, 026801 (2019).
- [33] B. Roy and V. Juričić, Unconventional superconductivity in nearly flat bands in twisted bilayer graphene, *Phys. Rev. B* **99**, 121407(R) (2019).
- [34] T. Huang, L. Zhang, and T. Ma, Antiferromagnetically ordered Mott insulator and $d + id$ superconductivity in twisted bilayer graphene: A quantum Monte Carlo study, *Sci. Bull.* **64**, 310 (2019).
- [35] S. Ray, J. Jung, and T. Das, Wannier pairs in superconducting twisted bilayer graphene and related systems, *Phys. Rev. B* **99**, 134515 (2019).
- [36] Y.-Z. You and A. Vishwanath, Superconductivity from valley fluctuations and approximate SO(4) symmetry in a weak coupling theory of twisted bilayer graphene, *npj Quantum Mater.* **4**, 16 (2019).
- [37] F. Wu, A. H. MacDonald, and I. Martin, Theory of Phonon-Mediated Superconductivity in Twisted Bilayer Graphene, *Phys. Rev. Lett.* **121**, 257001 (2018).
- [38] Y. W. Choi and H. J. Choi, Strong electron-phonon coupling, electron-hole asymmetry, and nonadiabaticity in magic-angle twisted bilayer graphene, *Phys. Rev. B* **98**, 241412(R) (2018).
- [39] B. Lian, Z. Wang, and B. A. Bernevig, Twisted Bilayer Graphene: A Phonon-Driven Superconductor, *Phys. Rev. Lett.* **122**, 257002 (2019).
- [40] C. L. Huang, N. M. Wei, W. Qin, and A. H. MacDonald, Pseudospin Paramagnons and the Superconducting Dome in Magic Angle Twisted Bilayer Graphene, *Phys. Rev. Lett.* **129**, 187001 (2022).
- [41] M. Xie and A. H. MacDonald, Nature of the Correlated Insulator States in Twisted Bilayer Graphene, *Phys. Rev. Lett.* **124**, 097601 (2020).
- [42] S. Liu, E. Khalaf, J. Y. Lee, and A. Vishwanath, Nematic topological semimetal and insulator in magic angle bilayer graphene at charge neutrality, *Phys. Rev. Res.* **3**, 013033 (2021).
- [43] J. Liu and X. Dai, Theories for the correlated insulating states and quantum anomalous Hall effect phenomena in twisted bilayer graphene, *Phys. Rev. B* **103**, 035427 (2021).
- [44] A. MacDonald, H. Akera, and M. Norman, Quantum mechanics and superconductivity in a magnetic field, *Aust. J. Phys.* **46**, 333 (1993).
- [45] Z. Hao, A. M. Zimmerman, P. Ledwith, E. Khalaf, D. H. Najafabadi, K. Watanabe, T. Taniguchi, A. Vishwanath, and P. Kim, Electric field-tunable superconductivity in alternating-twist magic-angle trilayer graphene, *Science* **371**, 1133 (2021).
- [46] Y. R. Zhang, R. Polski, C. Lewandowski, A. Thomson, Y. Peng, Y. J. Choi, H. Kim, K. Watanabe, T. Taniguchi, J. Alicea, F. von Oppen, G. Refael, and S. Nadj-Perge, Promotion of superconductivity in magic-angle graphene multilayers, *Science* **377**, 1538 (2022).
- [47] J. M. Park, Y. Cao, L.-Q. Xia, S. Sun, K. Watanabe, T. Taniguchi, and P. Jarillo-Herrero, Robust superconductivity in

- magic-angle multilayer graphene family, *Nat. Mater.* **21**, 877 (2022).
- [48] R. Bistritzer and A. H. MacDonald, Moiré bands in twisted double-layer graphene, *Proc. Natl. Acad. Sci. USA* **108**, 12233 (2011).
- [49] S. Carr, S. Fang, Z. Zhu, and E. Kaxiras, Exact continuum model for low-energy electronic states of twisted bilayer graphene, *Phys. Rev. Res.* **1**, 013001 (2019).
- [50] S. A. Fang, S. Carr, Z. Y. Zhu, D. Massatt, and E. Kaxiras, [arXiv:1908.00058](https://arxiv.org/abs/1908.00058).
- [51] M. Xie and A. H. MacDonald, Weak-Field Hall Resistivity and Spin-Valley Flavor Symmetry Breaking in Magic-Angle Twisted Bilayer Graphene, *Phys. Rev. Lett.* **127**, 196401 (2021).
- [52] Z. A. H. Goodwin, F. Corsetti, A. A. Mostofi, and J. Lischner, Twist-angle sensitivity of electron correlations in moiré graphene bilayers, *Phys. Rev. B* **100**, 121106(R) (2019).
- [53] F. Guinea and N. R. Walet, Electrostatic effects, band distortions, and superconductivity in twisted graphene bilayers, *Proc. Natl. Acad. Sci. USA* **115**, 13174 (2018).
- [54] Z. A. H. Goodwin, V. Vitale, F. Corsetti, D. K. Efetov, A. A. Mostofi, and J. Lischner, Critical role of device geometry for the phase diagram of twisted bilayer graphene, *Phys. Rev. B* **101**, 165110 (2020).
- [55] D. M. Basko and I. L. Aleiner, Interplay of Coulomb and electron-phonon interactions in graphene, *Phys. Rev. B* **77**, 041409(R) (2008).
- [56] M. Angeli and M. Fabrizio, Jahn-Teller coupling to moiré phonons in the continuum model formalism for small-angle twisted bilayer graphene, *Eur. Phys. J. Plus* **135**, 630 (2020).
- [57] O. Vafek and J. Kang, Renormalization Group Study of Hidden Symmetry in Twisted Bilayer Graphene with Coulomb Interactions, *Phys. Rev. Lett.* **125**, 257602 (2020).
- [58] G. D. Mahan, *Many-Particle Physics* (Kluwer Academic, New York, 2000).
- [59] J.-H. Chen, C. Jang, S. D. Xiao, M. Ishigami, and M. S. Fuhrer, Intrinsic and extrinsic performance limits of graphene devices on SiO₂, *Nat. Nanotechnol.* **3**, 206 (2008).
- [60] E. H. Hwang and S. Das Sarma, Acoustic phonon scattering limited carrier mobility in two-dimensional extrinsic graphene, *Phys. Rev. B* **77**, 115449 (2008).
- [61] D. K. Efetov and P. Kim, Controlling Electron-Phonon Interactions in Graphene at Ultrahigh Carrier Densities, *Phys. Rev. Lett.* **105**, 256805 (2010).
- [62] F. C. Wu, E. H. Hwang, and S. Das Sarma, Phonon-induced giant linear-in- T resistivity in magic angle twisted bilayer graphene: Ordinary strangeness and exotic superconductivity, *Phys. Rev. B* **99**, 165112 (2019).
- [63] M. Koshino and Y.-W. Son, Moiré phonons in twisted bilayer graphene, *Phys. Rev. B* **100**, 075416 (2019).
- [64] C. Lewandowski, D. Chowdhury, and J. Ruhman, Pairing in magic-angle twisted bilayer graphene: Role of phonon and plasmon umklapp, *Phys. Rev. B* **103**, 235401 (2021).
- [65] P. B. Allen and R. C. Dynes, Transition temperature of strongly coupled superconductors reanalyzed, *Phys. Rev. B* **12**, 905 (1975).
- [66] P. Morel and P. W. Anderson, Calculation of the superconducting state parameters with retarded electron-phonon interaction, *Phys. Rev.* **125**, 1263 (1962).
- [67] T. Sohler, M. Calandra, C.-H. Park, N. Bonini, N. Marzari, and F. Mauri, Phonon-limited resistivity of graphene by first-principles calculations: Electron-phonon interactions, strain-induced gauge field, and Boltzmann equation, *Phys. Rev. B* **90**, 125414 (2014).
- [68] I. Yudhistira, N. Chakraborty, G. Sharma, D. Y. H. Ho, E. Laksono, O. P. Sushkov, G. Vignale, and S. Adam, Gauge-phonon dominated resistivity in twisted bilayer graphene near magic angle, *Phys. Rev. B* **99**, 140302(R) (2019).
- [69] J. L. Mañes, Symmetry-based approach to electron-phonon interactions in graphene, *Phys. Rev. B* **76**, 045430 (2007).
- [70] B. Lian, Z.-D. Song, N. Regnault, D. K. Efetov, A. Yazdani, and B. A. Bernevig, Twisted bilayer graphene. IV. insulator ground states and phase diagram, *Phys. Rev. B* **103**, 205414 (2021).
- [71] B. A. Bernevig, B. Lian, A. Cowsik, F. Xie, N. Regnault, and Z.-D. Song, Twisted bilayer graphene V: Exact analytic many-body excitations in Coulomb Hamiltonians: Charge gap, Goldstone modes, and absence of Cooper pairing, *Phys. Rev. B* **103**, 205415 (2021).
- [72] K.-H. Bennemann and J. B. Ketterson, *Superconductivity: Volume 1: Conventional and Unconventional Superconductors Volume 2: Novel Superconductors* (Springer, Berlin, 2008).
- [73] A. Laturia, M. L. Van de Put, and W. G. Vandenberghe, Dielectric properties of hexagonal boron nitride and transition metal dichalcogenides: From monolayer to bulk, *npj 2D Mater. Appl.* **2**, 6 (2018).
- [74] J. M. Pizarro, M. Rösner, R. Thomale, R. Valentí, and T. O. Wehling, Internal screening and dielectric engineering in magic-angle twisted bilayer graphene, *Phys. Rev. B* **100**, 161102(R) (2019).
- [75] Z. A. H. Goodwin, F. Corsetti, A. A. Mostofi, and J. Lischner, Attractive electron-electron interactions from internal screening in magic-angle twisted bilayer graphene, *Phys. Rev. B* **100**, 235424 (2019).